Numerical prediction of sound emission of confined flows based on a hybrid approach

Paul Maurerlehner[1], Stefan Schoder[1], Johannes Tieber[2], Helfried Steiner[2], Günter Brenn[2], Manfred Kaltenbacher[1]

[1] *Institute of Fundamentals and Theory in Electrical Engineering, TU Graz, 8010 Graz, Austria, Email: paul.maurerlehner@tugraz.at*

[2] *Institute of Fluid Mechanics and Heat Transfer, TU Graz, 8010 Graz, Austria, Email: helfried.steiner@tugraz.at*

Abstract

Confined flows induce sound at certain flow conditions, which can become unpleasant in electric vehicles due to the absence of combustion noise. Such phenomena often occur in automotive engineering due to unfavorable flow-guiding geometries caused by the restricted installation space. On the one hand, the flow-induced sound is emitted at duct openings (e.g.,ventilation inside the passenger cabin) and on the other hand, due to vibroacoustic emission of the flow-guiding structure excited by the flow. The numerical simulation of this problem involves the interaction of a fluid flow, the confining structure, and a surrounding acoustic domain. In the present work, the hybrid aeroacoustic approach is applied to compute the flow-induced sound of a confined airflow through a straight pipe based on Lighthill's wave equation. First, the aeroacoustic source terms are computed by an incompressible Large-Eddy Simulation of a low Mach number flow. The propagation of the aeroacoustic sources is then simulated by the in-house finite-element (FE) solver openCFS, which allows for a coupling of the involved physical fields. The simulation results demonstrate the physical phenomena influencing the the radiated sound of a straight pipe without any obstacle.

Introduction

The absence of combustion noise in electric vehicles results in a dominance of other sources of sound, such as flow-induced sound in flow guiding components. The application of Computational Aeroacoustics (CAA) during the design phase is a promising way to meet the packaging requirements as well as the ambitious demand for passenger comfort. By coupling the computational fluid domain with the surrounding structural domain via coupling conditions on the interface, not only the sound generation and propagation within the fluid can be computed, but also the vibroacoustic sound emission of the flow-guiding structure can be simulated.

We propose a numerical model based on a hybrid (two-step) approach for the prediction of the sound emission of confined low Mach number flows (see Fig. 1) using Lighthill's wave equation. The first step of the simulation workflow is the computation of the aeroacoustic source terms by performing an incompressible Large-Eddy Simulation (LES) based on the finite-volume method. The propagation of the acoustic pressure waves, produced by the aeroacoustic sources, is then simulated by the in-house FE solver openCFS, which allows for a coupling of the aeroacoustic field, the structural mechanics domain of the confining solid structure, and the surrounding acoustic region.

The two-step approach allows to consider the mechanical coupling within the propagation simulation. Therefore, no additional computational workload is added to the computationally intensive Computational Fluid Dynamics (CFD) simulation by the mechanical coupling. As a result of this, back-coupling from the structure to the fluid flow is not modelled, whereas back-coupling from the structure to the acoustic domain is considered. Furthermore, boundary conditions (BCs) can be varied within the propagation simulation without the need for a new flow simulation if the changes do not impact the flow. This makes the approach efficient for optimization problems, such as the reduction of the radiated sound.

After introducing the methodology, it is applied in this paper to a turbulent low Mach number airflow through a straight aluminum pipe to predict the flow-induced sound and the vibroaoustic sound radiated to the surroundings. The results of the incompressible LES and the coupled acoustic propagation simulation are discussed, and finally, the conclusions are drawn.

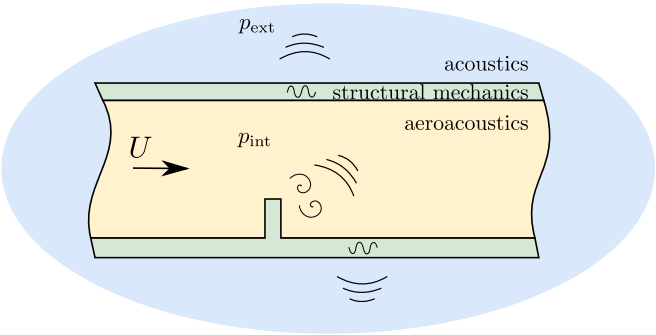

Figure 1: Sound generation and transmission mechanisms of a confined turbulent flow.

Methodology

The methodology for the CAA simulation is based on a hybrid approach, which divides the task of sound computation into a CFD simulation and a Computational Acoustic (CA) simulation (propagation simulation) as displayed in Fig. 2 [1]. As a part of this concept, the computed source terms are interpolated in a pre-processing step, where conservation of energy is enforced by considering the intersection of the CFD grid and the CA grid, as described in [2]. Furthermore, mean values of the source term are removed prior to the propagation simulation.

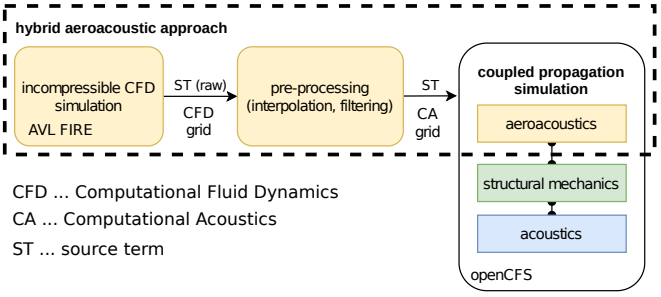

Figure 2: Simulation workflow based on the hybrid aeroacoustic approach.

Lighthill's inhomogeneous wave equation is used to compute the flow-induced sound in the propagation simulation. Considering the isentropic relation $p = c^2\rho$ between the pressure p and density ρ, it reads as

$$\frac{1}{c_0^2}\frac{\partial^2}{\partial t^2}\,p' - \Delta p' = \nabla\cdot\nabla\cdot[\boldsymbol{T}]\,, \tag{1}$$

which is referred to as the pressure formulation of Lighthill's wave equation. The partial differential equation (PDE) is solved for the pressure fluctuation $p'(t) = p(t) - p_0$ with p being the instantaneous pressure and p_0 the temporal mean value. In (1), c_0 denotes the speed of sound of the uniform medium.

The right-hand side of (1) is the Lighthill source term defined as the double divergence of the Lighthill stress tensor $[\boldsymbol{T}]$, which is provided by the CFD simulation. For low Mach number flows (Ma < 0.3), the Lighthill stress tensor is dominated by the Reynolds stress term, resulting in

$$[\boldsymbol{T}] = \rho_0 \boldsymbol{v}^{\mathrm{ic}} \otimes \boldsymbol{v}^{\mathrm{ic}}\,, \tag{2}$$

where ρ_0 is the mean density and $\boldsymbol{v}^{\mathrm{ic}}$ denotes the incompressible flow velocity. The weak form of the PDE (1) is derived by multiplying (1) with a test function φ, integrating over the computational domain Ω (see Fig. 3), and applying the Gauss Divergence Theorem

$$\frac{1}{c_0^2}\int_\Omega \varphi\frac{\partial^2}{\partial t^2}p'\mathrm{d}\Omega + \int_\Omega \nabla\varphi\cdot\nabla p'\mathrm{d}\Omega - \int_\Gamma \nabla p'\cdot\boldsymbol{n}\,\varphi\,\mathrm{d}\Gamma = \int_\Omega \nabla\cdot\nabla\cdot[\boldsymbol{T}]\,\varphi\,\mathrm{d}\Omega\,. \tag{3}$$

The relation

$$\nabla p' = -\rho_0\frac{\partial \boldsymbol{v}}{\partial t} - \nabla\cdot[\boldsymbol{T}]\,, \tag{4}$$

is substituted into the surface integral over the wall region Γ_W, which arises in the derivation of Lighthill's analogy from the balance of momentum [3]. The integrals over the inlet interface Γ_1 and the outlet interface Γ_2 are not changed. Due to the no-slip BC ($\boldsymbol{v}^{\mathrm{ic}} = 0$), the right-hand side of equation (4) vanishes on Γ_W so that equation (3) is rewritten as

$$\frac{1}{c_0^2}\int_\Omega \varphi\frac{\partial^2}{\partial t^2}p'\mathrm{d}\Omega + \int_\Omega \nabla\varphi\cdot\nabla p'\mathrm{d}\Omega + \int_{\Gamma_\mathrm{W}} \rho_0\frac{\partial \boldsymbol{v}}{\partial t}\cdot\boldsymbol{n}\,\varphi\,\mathrm{d}\Gamma = \int_{\Gamma_{1,2}} \nabla p'\cdot\boldsymbol{n}\,\varphi\,\mathrm{d}\Gamma + \int_\Omega \nabla\cdot\nabla\cdot[\boldsymbol{T}]\,\varphi\,\mathrm{d}\Omega\,. \tag{5}$$

The strong coupling with the structural mechanic domain on Γ_W is enforced by the kinematic coupling condition

$$\rho_0\frac{\partial\,\boldsymbol{v}}{\partial t}\cdot\boldsymbol{n} = \rho_0\,\frac{\partial^2\boldsymbol{u}_{\mathrm{mech}}}{\partial t^2}\,\cdot\,\boldsymbol{n}\,, \tag{6}$$

as well as the continuity of forces (dynamic coupling condition)

$$p'\boldsymbol{n} = -[\boldsymbol{\sigma}_{\mathbf{mech}}]\cdot\boldsymbol{n} \tag{7}$$

where $\boldsymbol{u}_{\mathrm{mech}}$ is the mechanical displacement and $[\boldsymbol{\sigma}_{\mathbf{mech}}]$ the stress tensor of the structural mechanic domain, which is governed classically by the balance of momentum and a linear stress-strain relationship. The boundaries Γ_1 and Γ_2 are modelled as adjacent perfectly matched layers (PML) to avoid reflections [4]. The external acoustic domain is governed by the acoustic wave equation, which is the homogeneous form of (1).

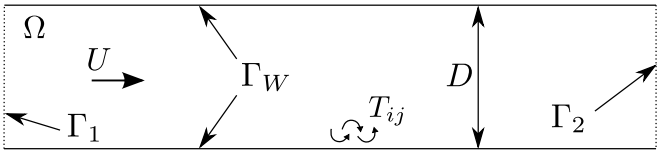

Figure 3: Computational aeroacoustic domain of the confined flow with exemplarily indicated sound sources in the wall shear layer.

Results

The above described workflow is applied to a fully developed turbulent airflow ($U = 3.9\,\frac{\mathrm{m}}{\mathrm{s}}$) through a straight aluminum pipe with an inner diameter of $D = 50$mm, a wall thickness of 3mm, and a length of 1.15m. Dry air at 23°C is considered for the flow domain and the external acoustic domain. The fluid density $\rho_{\mathrm{air}} = 1.176\,\frac{\mathrm{kg}}{\mathrm{m}^3}$, the dynamic viscosity $\mu_{\mathrm{air}} = 18.3\,\mu\mathrm{Pa\,s}$, and the speed of sound $c_{\mathrm{air}} = 345.2\,\frac{\mathrm{m}}{\mathrm{s}}$ are chosen as the required material parameters for the simulations. At both ends of the pipe, flexible, movable mounts are considered with a mounting stiffness of k_x, k_y, and k_z in x, y, and z direction, respectively. The material parameters for the aluminum pipe and the two mounting regions are shown in Tab. 1.

Table 1: Structural mechanic material parameters.

material	Young's modulus	Poisson ratio	density
aluminum	70GPa	0.33	$2\,700\,\frac{\mathrm{kg}}{\mathrm{m}^3}$
mount	110MPa	0.30	$1\,000\,\frac{\mathrm{kg}}{\mathrm{m}^3}$

Incompressible flow simulation

The incompressible Navier-Stokes equations are solved by LES in AVL FIRE based on the finite-volume (FV) method. At the inlet face, a turbulent fluctuating velocity distribution was prescribed, which was generated in a precursor LES, considering fully developed, axially periodic, turbulent flow through a 5D long pipe. At the outflow boundary, an averaged pressure BC was used. The computational grid of the $25D$ long cylinder consisted of about 3.9 million FV cells. Figure 4 presents the cross-sectional view of half the CFD mesh, where a near-wall resolution of $y^+ = 0.076$ was achieved. The time step size

set to 10 µs, and the simulation time was 0.2 s. The instantaneous Lighthill source term $\nabla \cdot \nabla \cdot [\boldsymbol{T}]$ is illustrated in Fig. 5. In the considered straight pipe flow, the source terms are mainly produced in the highly sheared near-wall region, where the production of turbulent kinetic energy becomes maximum. The predicted source terms were further interpolated onto the multiphysics mesh for the subsequent coupled propagation simulation.

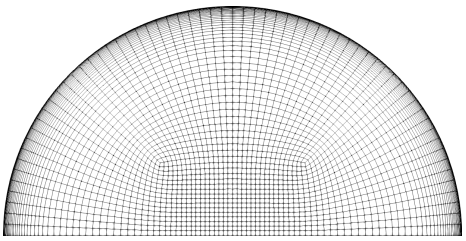

Figure 4: Cross-sectional view of the upper half of the CFD mesh.

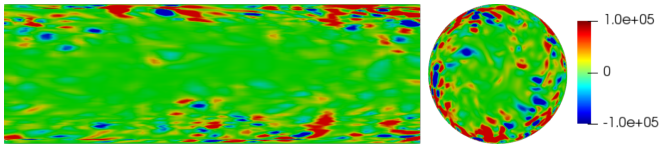

Figure 5: Contours of the instantaneous Lighthill source term in $\frac{\mathrm{kg}}{\mathrm{s}^2\,\mathrm{m}^3}$ in meridional and cross-sectional cutting planes.

Propagation simulation

The above derived weak form of Lighthill's wave equation with the respective coupling and boundary conditions is solved by the multiphysics solver openCFS, applying the FE method [5]. The same temporal resolution as in the CFD simulation was chosen, and a zero initial condition was used. In Fig. 6, a detail of the clipped multiphysics mesh is displayed. The mesh consists of the internal aeroacoustic domain (red), which includes the aeroacoustic sources, the structural mechanics domain of the mounts (green) and the pipe (pink), and the surrounding acoustic domain (blue). Additionally, adjacent PML regions (yellow) avoid reflections at the boundaries and ensure free field conditions for the external fluid domain. At the external coupling interface of the pipe, a non-conforming (NC) grid technique based on Nitsche-type mortaring according to [6] was used to guarantee a flexible meshing and a reduced number of elements. At the surfaces of the mounting regions, a normal acting stiffness was prescribed in accordance with the above defined mounting stiffnesses k_x, k_y, and k_z. The total number of elements sums up to 224 600, and the maximum element size is 6 mm (see Tab. 2), resolving acoustic waves up to $f_\mathrm{max} = 7$ kHz by at least 8.16 finite elements within the external fluid. Linear elements were used for the aeroacoustic and acoustic domain, while quadratic FE basis functions are applied to the structural mechanics domain.

The shown spectral results were obtained by averaging over the spectra of a grid of evaluation points, located

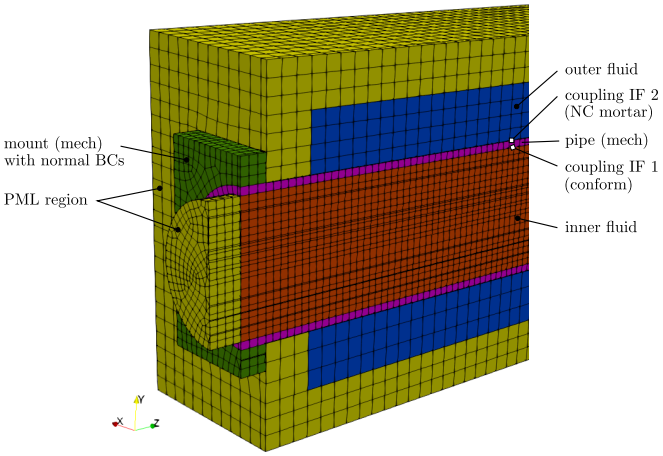

Figure 6: FE simulation setup for the coupled propagation simulation.

Table 2: Details of the multiphysics mesh.

region	no. regions	no. cells	cell size	el. order
int. fluid	1	116 000	3mm	1
ext. fluid	1	35 700	6mm	1
PML (ext.)	1	46 300	6mm	1
PML (int.)	2	1 200	3mm	1
pipe	1	22 200	3mm	2
mount	2	1 000	3mm	2
total	8	224 600	3-6mm	-

in the internal and external fluid domains, respectively. The internal pressures are evaluated on the pipe wall, while the external acoustic pressure is assessed 10mm radially away from the external pipe wall (see Fig. 7). The uniform evaluation grid consists of 8 points in the circumferential, and 10 points in the axial direction of the pipe. The spectral pressure level (PL) of the internal

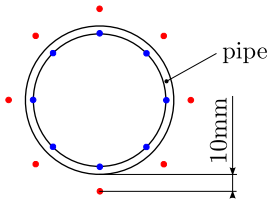

Figure 7: Positions of the internal near-wall (blue) and external (red) evaluation points.

fluid and the spectral sound pressure level (SPL) of the external fluid obtained, from the Fast Fourier Transform (FFT) of the time signals with a reference pressure $p_\mathrm{ref} = 20\,\mu$Pa, are illustrated in Fig. 8 and Fig. 9, respectively.

Figure 8 compares the averaged spectra of the internal wall pressure of the incompressible flow simulation against the results from the propagation simulation. Apart from the two peaks, the spectrum of the CFD simulation is reproduced by the propagation simulation.

The two peaks indicate the excitation of higher-order acoustic modes at the eigenfrequency f_mn, where m denotes the circumferential order and n the radial order.

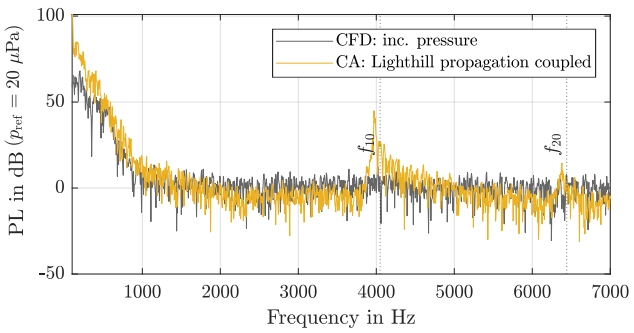

Figure 8: Averaged spectrum of the internal wall pressure fluctuations.

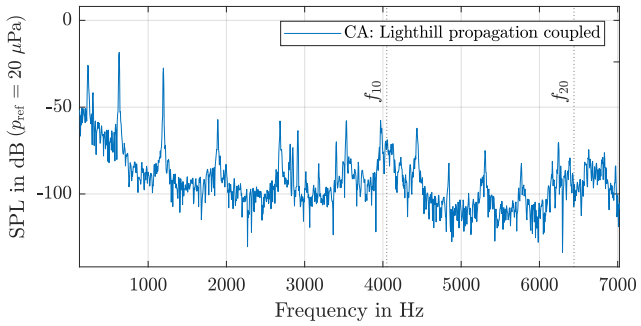

Figure 9: Averaged spectrum of the radiated sound.

The mode shapes of the two transversal pipe modes, which occur within the considered frequency range, are shown in Fig. 10. These modes are resolved by the propagation simulation, because Lighthill's wave equation considers aerodynamic and acoustic effects. The peaks within the spectrum of the radiated sound close to f_{10} and f_{20} in Fig. 9 reveal that the acoustic pressure fluctuations due to the transversal pipe modes are transmitted by the flow confining structure. Further peaks within the spectrum indicate the excitation of structural modes of the pipe. These structural modes include, for example, bending modes of several orders and also rigid-body modes due to the movable mounts. Without the free-field condition, acoustic room modes could also occur within the external acoustic domain. When comparing the spectra of the internal (Fig. 8) and external (Fig. 9) pressure fluctuations, an overall reduction of the pressure fluctuations through the pipe wall of about 100dB can be identified. Since the SPL of the radiated sound is significantly below the threshold of human hearing, the present application is not relevant for practice. However, the results demonstrate the physical effects which impact the radiated sound of confined flows.

Conclusions

A methodology to predict the aeroacoustic sound generation and vibroacoustic sound emission of confined flows for small structural deformations and low Mach number was introduced. The methodology is based on the hybrid aeroacoustic approach and utilizes Lighthill's wave equation for computing the flow-induced sound. The coupling of the internal aeroacoustic domain with the structural

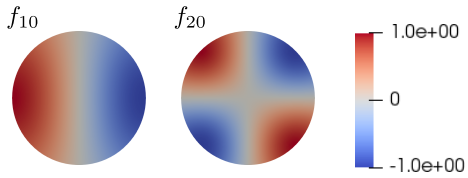

Figure 10: Mode shapes of the first two transversal acoustic pipe modes (normalized acoustic pressure).

mechanics domain of the flow confining structure and an external purely acoustic domain enables the computation of the sound radiated to the surroundings. The application to the flow through a straight aluminum pipe shows that the radiated sound depends on the acoustic source terms resulting from the flow, the acoustic properties of the internal fluid domain, and the mechanical properties of the flow guiding structure. The latter can be varied within the propagation simulation without the need for a new flow simulation, which makes the methodology well suited for numerical optimization. For example, the radiated sound can be influenced by considering absorbing materials, the mounting conditions of the structure can be adapted, or the structure itself can be optimized with regard to the radiated sound. The analysis of the source terms predicted by the LES shows that the aeroacoustic source terms originate in a straight pipe (without any obstacle) mainly from the high shear rate in the near-wall region.

References

[1] Stefan Schoder and Manfred Kaltenbacher. Hybrid aeroacoustic computations: State of art and new achievements. *Journal of Theoretical and Computational Acoustics*, 27(4):1950020, 2019.

[2] S. Schoder, C. Junger, M. Weitz, and M. Kaltenbacher. Conservative source term interpolation for hybrid aeroacoustic computations. In *25th AIAA/CEAS Aeroacoustics Conference*, 2019-2538, 2019.

[3] Michael James Lighthill. On sound generated aerodynamically I. general theory. *Proceedings of the Royal Society of London. Series A. Mathematical and Physical Sciences*, 211(1107):564–587, 1952.

[4] Barbara Kaltenbacher, Manfred Kaltenbacher, and Imbo Sim. A modified and stable version of a perfectly matched layer technique for the 3-d second order wave equation in time domain with an application to aeroacoustics. *Journal of computational physics*, 235:407–422, 2013.

[5] Finite element multiphysics solver openCFS. opencfs.org, 2021.

[6] Manfred Kaltenbacher and Sebastian Floss. Nonconforming finite elements based on nitsche-type mortaring for inhomogeneous wave equation. *Journal of theoretical and computational acoustics*, 26(03):1850028, 2018.